Probing the electronic structure and Au–C chemical bonding in AuC2 and AuC2 using high-resolution photoelectron spectroscopy

Iker León, Zheng Yang, and Lai-Sheng Wang

Citation: The Journal of Chemical Physics **140**, 084303 (2014); doi: 10.1063/1.4865978
View online: http://dx.doi.org/10.1063/1.4865978
View Table of Contents: http://scitation.aip.org/content/aip/journal/jcp/140/8?ver=pdfcov
Published by the AIP Publishing

Probing the electronic structure and Au–C chemical bonding in AuC_2^- and AuC_2 using high-resolution photoelectron spectroscopy

Iker León, Zheng Yang, and Lai-Sheng Wang[a)]
Department of Chemistry, Brown University, Providence, Rhode Island 02912, USA

(Received 24 December 2013; accepted 5 February 2014; published online 24 February 2014)

We report photoelectron spectroscopy (PES) and high-resolution PE imaging of AuC_2^- at a wide range of photon energies. The ground state of AuC_2^- is found to be linear ($C_{\infty v}$, $^1\Sigma^+$) with a $\ldots 8\pi^4 4\delta^4 17\sigma^2 9\pi^4 18\sigma^2$ valence configuration. Detachments from all the five valence orbitals of the ground state of AuC_2^- are observed at 193 nm. High-resolution PE images are obtained in the energy range from 830 to 330 nm, revealing complicated vibronic structures from electron detachment of the 18σ, 9π, and 17σ orbitals. Detachment from the 18σ orbital results in the $^2\Sigma^+$ ground state of neutral AuC_2, which, however, is bent due to strong vibronic coupling with the nearby $^2\Pi$ state from detachment of a 9π electron. The $^2\Sigma^+$–$^2\Pi$ vibronic and spin-orbit coupling results in complicated vibronic structures for the $^2\Sigma^+$ and $^2\Pi_{3/2}$ states with extensive bending excitations. The electron affinity of AuC_2 is measured accurately to be 3.2192(7) eV with a ground state bending frequency of 195(6) cm^{-1}. The first excited state ($^2A'$) of AuC_2, corresponding to the $^2\Pi_{3/2}$ state at the linear geometry, is only 0.0021 eV above the ground state ($^2A'$) and has a bending frequency of 207(6) cm^{-1}. The $^2\Pi_{1/2}$ state, 0.2291 eV above the ground state, is linear with little geometry change relative to the anion ground state. The detachment of the 17σ orbital also results in complicated vibronic structures, suggesting again a bent state due to possible vibronic coupling with the lower $^2\Pi$ state. The spectrum at 193 nm shows the presence of a minor species with less than 2% intensity relative to the ground state of AuC_2^-. High-resolution data of the minor species reveal several vibrational progressions in the Au–C stretching mode, which are assigned to be from the metastable $^3\Pi_{2,1,0}$ spin-orbit excited states of AuC_2^- to the $^2\Pi_{3/2,1/2}$ spin-orbit states of neutral AuC_2. The spin-orbit splittings of the $^3\Pi$ and $^2\Pi$ states are accurately measured at the linear geometry. The current study provides a wealth of electronic structure information about AuC_2^- and AuC_2, which are ideal systems to investigate the strong Σ–Π and spin-orbit vibronic couplings. © *2014 AIP Publishing LLC*. [http://dx.doi.org/10.1063/1.4865978]

I. INTRODUCTION

Due to the strong relativistic effects,[1] gold displays many unique chemical properties, such as aurophilicity and propensity to form covalent bonds.[2–4] The covalent bonding character in gold-containing molecules has been increasingly recognized in the chemistry of gold. The Au–C bonding has, in particular, been very important in homogeneous catalysis involving gold, which has been a subject of growing interest over the last decade.[5–9] Recently, in order to understand the nature of the bonding between Au and substrates involving C≡C triple bonds, we have investigated, using photoelectron spectroscopy (PES) and theoretical calculations,[10] a series of Au(I)-alkynyl complexes, $LAuCCH^-$ (L = Cl, I, CCH), produced using an electrospray ionization source. We observed an unusually large Au–C stretching frequencies in these complexes, leading to the surprising finding that the Au–C bond in these complexes is extremely strong with a dissociation energy of 5.01 eV in $ClAuCCH^-$. Even more surprisingly, we found that the Au–C single bond in $ClAuCCH^-$ is even stronger than the Au=C double bond in $ClAu{=}CH_2$ and the Au≡C triple bond in ClAu≡C, revealing an inverse correlation between bond strength and bond orders in the series of Au–C compounds. The auxiliary ligand L is found to polarize the Au^I center in $ClAuCCH^-$, resulting in the unusually strong Au–C bond. To understand the polarization effects, it would be desirable to study the bonding in Au-CCH or the isoelectronic Au-CC^- species, which can serve as a reference to compare with the Au–C bonding in the $LAuCCH^-$ complexes. In the current paper, we present a study on the electronic structure and chemical bonding in Au–CC^- and Au–CC using high-resolution PES and PE imaging.

There has been scarce experimental information about gold-carbon clusters. Apart from mass spectrometric observations of the $Au_nC_m^+$ and $Au_nC_m^-$ species,[11,12] there is no experimental structural or spectroscopic information on any Au–C clusters, except a very recent PES and computational study on AuC_2^-.[13] In this work, Visser *et al.*[13] reported interesting PE imaging on AuC_2^- in the photon energy range from 610 nm to 585 nm, showing a single vibrational progression starting at an electron binding energy of 1.442 eV with a vibrational frequency of 528 cm^{-1} due to the Au–C stretching in neutral AuC_2. Surprisingly, the observed spectral features were assigned to derive from a highly excited state of AuC_2^-, whereas the electron binding energies of the ground state of AuC_2^- were suggested to be too high to be

a)E-mail: Lai-Sheng_Wang@brown.edu

accessible with their available photon energies. The accompanying calculations showed that the anion ground state of AuC_2^- is a linear molecule with a $^1\Sigma^+$ electronic state and a closed-shell valence electron configuration of $8\pi^4 4\delta^4 17\sigma^2 9\pi^4 18\sigma^2$, whereas the neutral ground state is bent with a $^2A'$ electronic state derived from detaching an 18σ electron. The observed spectral features were assigned to be from a $^3A'$ bent excited state of AuC_2^- derived from the $\ldots 9\pi^4 18\sigma^1 19\sigma^1$ electron configuration. The energy of this excited state was calculated to be 1.15 eV above the linear ground state of AuC_2^-. A linear $^3\Pi$ excited state derived from the $\ldots 9\pi^3 18\sigma^2 19\sigma^1$ configuration was also calculated to be close in energy at 1.18 eV above the anionic ground state. At first glance, it seems extremely improbable that such a highly excited anion was observed.

Over the past decade, PE imaging has been developed into a highly sophisticated new PES technique for negative ions.[14,15] It not only yields photoelectron angular distributions, but also allows very high resolution spectra to be obtained. We have recently developed a high-resolution PE imaging capability.[16–18] In the current study, we apply this technique to AuC_2^- at a much more extended photon energy range. PES spectra from the linear ground state of AuC_2^- are obtained for the first time and detachment transitions from all five valence orbitals of AuC_2^- are observed at 193 nm using our magnetic-bottle PES apparatus. High-resolution PE imaging data are obtained for the first three detachment channels of AuC_2^-. Strong vibronic coupling is observed between the $^2\Sigma^+$ ground state of AuC_2 and the $^2\Pi_{3/2}$ spin-orbit state of the $^2\Pi$ excited state, resulting in two bent states (both of $^2A'$ symmetry) and extremely complicated vibronic features. The adiabatic detachment energy (ADE) to the A′ bent ground state of AuC_2 is at 3.2192 eV, which gives accurately the electron affinity (EA) of AuC_2. The excited A′ ($^2\Pi_{3/2}$) state is almost degenerate with the ground state, only 0.0021 eV higher, with an ADE of 3.2213 eV. The $^2\Pi_{1/2}$ spin-orbit state (ADE: 3.4483 eV) is observed to be linear with little geometry change relative to the anion ground state. The excited state derived from electron detachment from the 17σ orbital is also found to be bent with an ADE of 3.5725 eV.

The excited electronic state of the AuC_2^- anion was observed in our 193 nm spectrum with a population of less than 2% relative to the linear ground state, as a "spin-protected" metastable excited state. We have also obtained high-resolution PE imaging data from this very weakly populated excited anion. More interestingly, our high-resolution capability leads to a different spectral assignment from that proposed by Visser *et al.*[13] The observed detachment transitions are assigned to be from the $^3\Pi_{2,1,0}$ ($\ldots 9\pi^3 18\sigma^2 19\sigma^1$) anionic excited states to the $^2\Pi_{3/2,1/2}$ ($\ldots 9\pi^3 18\sigma^2$) neutral final states. The energies of the three spin-orbit states of the anion excited state are measured to be 1.8089 eV ($^3\Pi_2$), 1.8646 eV ($^3\Pi_1$), and 1.9047 eV ($^3\Pi_0$) relative to the ground state. The spin-orbit coupling constant of the $^2\Pi$ excited state of neutral AuC_2 at the linear geometry is measured to be 879 cm^{-1}. The current study allows the electronic structure and spectroscopy of AuC_2^- and AuC_2 to be well characterized, demonstrating the power of high-resolution PE imaging.

II. EXPERIMENTAL AND THEORETICAL METHODS

A. Experimental methods

The experiments were done using two different PES instruments, which employ similar laser vaporization supersonic cluster sources and time-of-flight mass spectrometry for cluster generation and size selection, but different photoelectron detections, one with a magnetic-bottle apparatus[19] for the high photon energy experiment at 193 nm and the other one involving a recently built velocity-map imaging (VMI) system.[16–18] For both experiments, a disk made of C and Au (C/Au atom ratio ~1/9) was used as the laser vaporization target with a helium carrier gas seeded with 10% argon, which was shown to produce relatively cold gold cluster anions previously.[20] Clusters formed inside the nozzle were entrained by the carrier gas and underwent a supersonic expansion. After a skimmer, anions from the collimated cluster beam were extracted perpendicularly into a time-of-flight mass spectrometer. The AuC_2^- anion of current interest was mass-selected and decelerated before being detached by a 193 nm laser beam in the interaction zone of the magnetic-bottle electron analyzer, which were described in detail before.[19] The pulsed laser beam at 193 nm (6.424 eV) was from an ArF excimer laser. Photoelectrons were collected at nearly 100% efficiency by the magnetic bottle and analyzed in a 3.5 m long electron flight tube. The spectrum was calibrated with the known spectrum of Bi^-. The kinetic energy resolution of the apparatus, $\Delta Ek/Ek$, was better than 2.5%, i.e., 25 meV for 1 eV electrons.

For the high-resolution PES experiment, the AuC_2^- anion was mass-selected and focused into a collinear VMI system for photodetachment by a tunable laser.[16–18] Photoelectrons were accelerated toward a position-sensitive detector with a 75 mm diameter micro-channel plate coupled to a phosphor screen and a charge-coupled device (CCD) camera. A National Instrument PXI-mainframe system was used to control the whole apparatus and for data acquisition. The tunable radiation (222–709 nm, linewidth <0.3 cm^{-1}) was from a Continuum Sunlite OPO system pumped by an injection-seeded Continuum Powerlite laser. Typical pulse energies used were ~150 μJ. A half-wave plate combined with a high-quality Glan-Laser polarizer was used to achieve a high degree of polarization parallel to the imaging detector plane. The electron count rates for the current experiment at certain wavelengths were very low and photoelectron images were averaged with 300 000–700 000 laser shots. Inverse-Abel transformation was done to obtain the three-dimensional (3D) electron distributions from the recorded two-dimensional (2D) images. This reconstruction was done by both the BASEX[21] and pBASEX[22] programs, which yielded similar results. The imaging system was calibrated using the known spectrum of Au^-.

B. Theoretical methods

Theoretical calculations were performed on AuC_2^- with the Gaussian 09 program package[23] using the B3LYP DFT method.[24,25] The all-electron 6-31++G(d,p) basis sets were

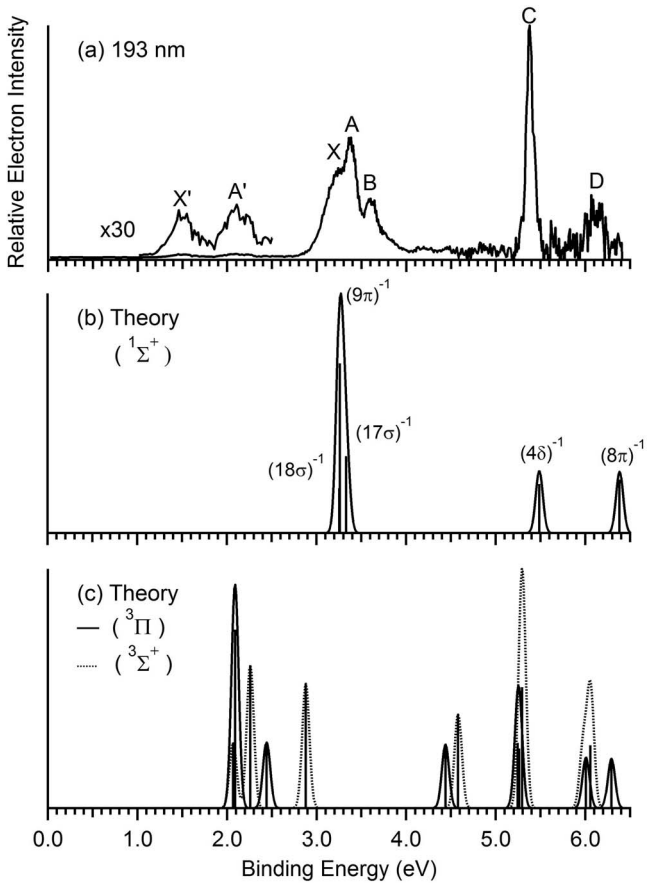

FIG. 1. (a) Photoelectron spectrum of AuC_2^- at 193 nm (6.424 eV). (b) Simulated spectrum for the ground state of AuC_2^- ($^1\Sigma^+$). (c) Simulated spectra from two triplet excited states of AuC_2^-. The vertical detachment energies for each state (represented by vertical bars) were calculated using TD-DFT and the simulated spectra were obtained by fitting a Gaussian function with a width of 0.04 eV to each VDE.

used for the carbon atoms, and the Lanl2dz basis set and associated effective core potential (ECP) were used for gold during the optimization calculations. Vibrational frequencies were calculated to confirm that the obtained structures were true minima (or to find imaginary frequencies if the structures were saddle points). Zero-point energy (ZPE) corrections were included for all the calculated energies.

Vertical detachment energies (VDEs) were calculated for the ground state and two excited states of AuC_2^- to compare with the experimental data. The first VDE was calculated as the energy difference between the anion and neutral states at the corresponding anion equilibrium geometry. Excitation energies of the neutral species were calculated at the anion geometry using the TD-DFT method and added to the first VDE to approximate the VDEs for the inner occupied orbitals of the anion.[26] The simulated spectra in Fig. 1 were obtained by fitting each of the computed VDEs with a Gaussian function of 0.04 eV width.

C. Angular distribution and the anisotropy parameter (β)

One of the most important advantages of PE imaging is that it gives the angular distributions of the photoelectrons, in addition to its high-resolution capability. For one-photon detachment, an anisotropy parameter (β) is calculated from the reconstructed PE images by analyses of the photoelectron differential cross-sections given by[27]

$$d\sigma/d\Omega = d\sigma_{total}/4\pi[1 + \beta P_2(\cos\ \theta)] \quad (1)$$

and thus the photoelectron angular distribution (PAD) is given by

$$dI(\theta) \sim [1 + \beta P_2(\cos\theta)], \quad (2)$$

where $P_2(\cos\ \theta) = \frac{1}{2}(3\cos^2\ \theta - 1)$ is the second order Legendre polynomial and θ measures the angle between the direction of the detachment laser polarization and that of the ejected electron. The anisotropy parameter represents the degree of alignment between the direction of the photodetached electrons and the polarization of the detachment laser, i.e., it provides information about the orbital angular momentum l of the ejected photoelectrons. It is numerically confined in the region $-1 \le \beta \le 2$. Typically, a single-electron model describes reasonably well the experimental observations. For example, for detachment from a pure atomic s-orbital, $\beta = 2$ corresponding to an anisotropic PAD with the maximum of intensity parallel with the photodetachment laser polarization. If the photoemission state is different from a pure s-orbital (s+d orbital, for instance), then partial wave interference can result in $\beta = -1$, corresponding to an anisotropic PAD with the maximum of intensity perpendicular to the detachment laser polarization. Detachment from atomic p-orbitals generates partial electron waves with d and s angular momenta, and usually for high kinetic energy electrons (above 1 eV), β will converge to 0 (isotropic) for pure s-wave or 1 for pure d-wave.

III. RESULTS

A. Photoelectron spectrum at 193 nm

Fig. 1(a) shows the PE spectrum of AuC_2^- at 193 nm using the magnetic-bottle apparatus. Several intense detachment bands are observed and labeled with letters X, A–D. The first three intense bands are fairly close to each other with VDEs at ~3.2 eV (X), ~3.4 eV (A), and ~3.6 eV (B). At higher binding energies, two more bands are observed: a very intense and sharp feature at 5.40 eV (C) and a weaker band at ~6.1 eV (D) with somewhat poor signal-to-noise ratios. The VDEs and ADEs of the observed bands are given in Table I, where the more accurate data for bands X, A, and B are from the high-resolution imaging data to be presented below.

Two very weak bands are also observed in the lower binding energy region, as seen more clearly in the inset of Fig. 1(a): feature X′ at ~1.5 eV and feature A′ at ~2.1 eV. The relative intensities of these features are no more than ~2% of the main spectral bands. The X′ band is consistent with the PE imaging data reported recently by Visser *et al.*[13] and hence should be due to the putative electronically excited AuC_2^- anion. Figs. 1(b) and 1(c) show the simulated spectra for detachment from the AuC_2^- ground state and its electronically excited states, respectively, confirming the presence of the excited anion. These results will be discussed in Sec. IV A.

TABLE I. Experimental adiabatic (ADE) and vertical (VDE) detachment energies from the ground state of AuC_2^-, their assignments, and comparison with calculated VDEs.

Observed feature	Final state	ADE (eV) experimental	VDE (eV) Experimental	VDE (eV) Theoretical[a]
X	$^2A'$ ($^2\Sigma^+$)	3.2192 ± 0.0007	3.2674 ± 0.0007	3.25
	$^2A'$ ($^2\Pi_{3/2}$)	3.2213 ± 0.0007	3.2722 ± 0.0007	3.26
A	$^2\Pi_{1/2}$	3.4483 ± 0.0007	3.4483 ± 0.0007	
B	$^2\Sigma$	3.5725 ± 0.0007	3.5932 ± 0.0012	3.33
C	$^2\Delta$		5.40 ± 0.03	5.48
D	$^2\Pi$		6.1 ± 0.1	6.37

[a]The calculation was done at DFT level using B3LYP with basis set 6-31++g(d,p) for C and Lanl2dz for Au. The calculations were done without spin-orbit coupling.

B. High resolution photoelectron imaging of bands X, A, and B

The PE image and spectrum at 3.6906 eV photon energy are shown in Fig. 2(a), covering the spectral region of the three strong bands X, A, and B revealed in the 193 nm spectrum. A great number of vibrational fine features (labeled as *a* to *g*) are resolved for band X, suggesting a large geometry change between the ground state of AuC_2^- and that of its neutral ground state. These peaks are separated by about 195 cm^{-1}, which should be due to the bending mode. The peaks from *a* to *f* resemble a typical Franck-Condon envelope in the bending coordinate, suggesting that the neutral ground state is likely bent in agreement with the recent calculation by Visser *et al.*[13] The band A in the 193 nm spectrum is resolved into a single sharp and intense peak at 3.4483 eV. The band B is resolved into four vibrational fine features between 3.57 and 3.67 eV, labeled as *i*, *j*, *k*, and *l* in Fig. 2(a). The *i*, *j*, *k* peaks appear to be due to a bending progression with an extremely large anharmonicity, because the spacing between *i* and *j* is 180 cm^{-1} and that between *j* and *k* is 150 cm^{-1}. The pattern of band B is similar to that of band X, both displaying a progression in the bending mode (features *a–f* in band X and features *i–k* in band B) and then a separated peak (feature *g* in band X and feature *l* in band B). The peaks *i*, *j*, *k* seem to contain fine features in the 3.6906 eV spectrum (Fig. 2(a)). When taken at a slightly lower photon energy of 3.6297 eV, these three peaks are each resolved into a doublet (inset of Fig. 2(a)), which are labeled as i_1/i_2, j_1/j_2, and k_1/k_2.

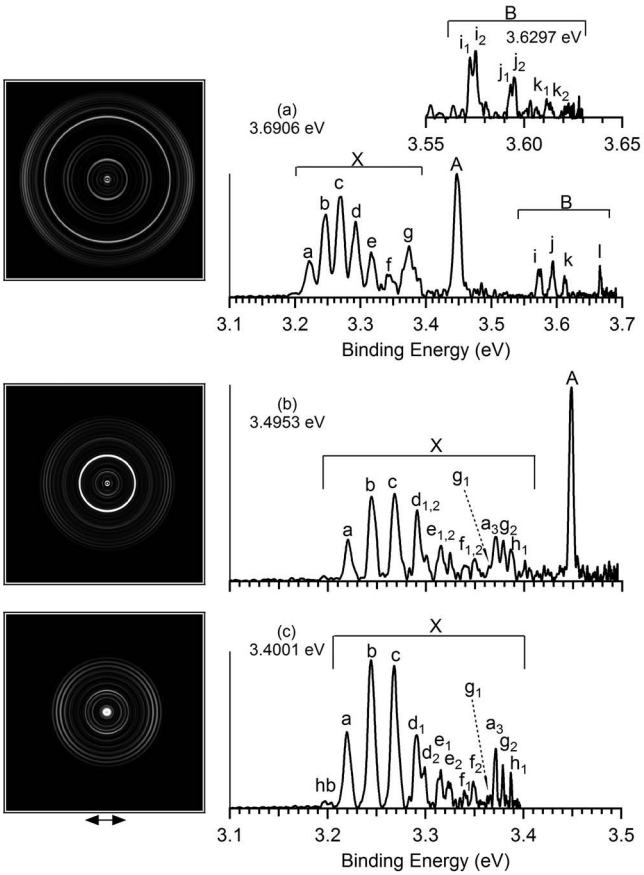

FIG. 2. High-resolution photoelectron images and spectra of AuC_2^- at detachment photon energies of (a) 3.6906 eV, (b) 3.4953 eV, (c) 3.4001 eV. The inset in (a) is taken at a photon energy of 3.6297 eV. The left panels show the photoelectron images after inverse-Abel transformation. The double arrow indicates the polarization of the laser.

When the detachment laser is set to 3.4953 eV, which is closer to band A (Fig. 2(b)), the spectral resolution is improved for both bands X and A. Still, only a single peak is observed for band A with a peak width of about 40 cm^{-1}, which is higher than the spectral resolution, but there is no hint of any fine features. Hence, band A must represent a detachment transition to an excited state of AuC_2 with nearly identical structure as the AuC_2^- ground state. On the other hand, the peak *g* of band X is resolved into four fine features separated by about 60 cm^{-1} (labeled as g_1, a_3, g_2, and h_1). Additionally, peaks *d*, *e*, and *f* are also each resolved unexpectedly into two features (d_1/d_2, e_1/e_2, f_1/f_2, respectively). Fig. 2(c) at 3.4001 eV photon energy confirms the observation of the fine features with even better resolution, although the g_1 fine feature appears to be very weak. We should also point out that in each of the three spectra shown in Fig. 2 there is also a very weak feature near 3.2 eV due to a vibrational hot band (labeled as hb in Fig. 2(c)). The almost negligibility of this feature suggests that our cluster beam is quite cold vibrationally.

To further improve the resolution for the spectral features of band X, we have taken a series of PE images by setting the detachment energy close to each of the vibrational peaks, as shown in Fig. 3. Interestingly, every vibrational peak in

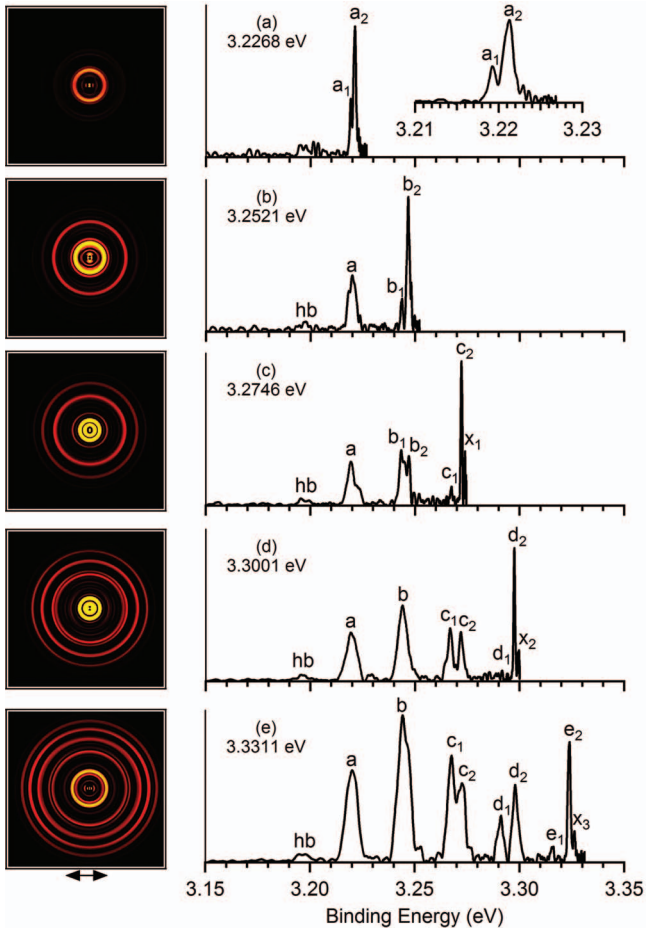

FIG. 3. High-resolution photoelectron images and spectra of AuC_2^- at detachment photon energies of (a) 3.2268 eV, (b) 3.2521 eV, (c) 3.2746 eV, (d) 3.3001 eV, and (e) 3.3311 eV. The left panels show the photoelectron images after inverse-Abel transformation. The double arrow indicates the polarization of the laser. The inset in (a) shows an expanded view of the a_1 and a_2 peaks.

band X is now resolved into a doublet, labeled as a_1/a_2, b_1/b_2, c_1/c_2, d_1/d_2, and e_1/e_2. It is observed that the spacing between each of the doublet is not constant and it seems to increase for the higher binding energy peaks. However, the separation between successive peaks of the lower component of each doublet (i.e., a_1, b_1, c_1, d_1 ...) seems to be constant with a spacing of 195 ± 6 cm^{-1}. The separation between the peaks of the higher energy component of each doublet (i.e., a_2, b_2, c_2, d_2 ...) is also constant with a slightly larger spacing of 207 ± 6 cm^{-1}. Additionally, starting from peak c in Fig. 3(c), a new peak is observed as a shoulder very near the threshold (labeled as x_1, x_2, and x_3 in Figs. 3(c)–3(e), respectively). However, these features are very weak and close to the center of the image and thus we cannot be sure whether they are real spectral features or artifacts from the image inversion. The hot band is also resolved more clearly in Fig. 3 and it is separated from the peak a by about 195 cm^{-1}, which should be the bending frequency of the AuC_2^- ground state. It should be noted that the hot band has been confirmed by varying the expansion conditions of our cluster source.

Thus, the doublet features of the X band must represent two nearly degenerate electronic states of neutral AuC_2, which are both bent. The a_1, b_1, c_1, d_1 ... components should correspond to the bending vibrations of the ground electronic state of AuC_2. Hence, the a_1 peak represents the ADE from the ground state of the anion to that of the neutral and defines accurately the EA of AuC_2 as 3.2192(7) eV. The a_2, b_2, c_2, d_2 ... peaks represent the first excited state of AuC_2, which is only 0.0021 eV (the separation between the a_1 and a_2 components of peak a in Fig. 3) above the ground state with a slightly higher bending frequency. That these two sets of peaks correspond to two different electronic states is confirmed by their very different threshold behaviors in Fig. 3. The intensities of the vibrational features of the ground state (a_1–e_1) are drastically decreased near threshold, whereas those of the closely-lying higher state (a_2–e_2) are enhanced near threshold. However, away from the threshold, the relative intensities of the ground state vibrational peaks are higher.

The different electronic nature of these two states is also reflected in their very different angular distributions. The different angular distributions of the two components can be seen from the PE images already, in particular, for the well resolved c_1/c_2 peaks in Fig. 3(d) and the d_1/d_2 peaks in Fig. 3(e). The c_1 and d_1 peaks both display parallel PAD with maximum intensities along the laser polarization, whereas the c_2 and d_2 peaks show more isotropic PAD. The anisotropy parameter has been obtained for each component from the high-resolution PE images by fitting the PAD with Eq. (2). Fig. 4 shows the β parameter at different kinetic energies for

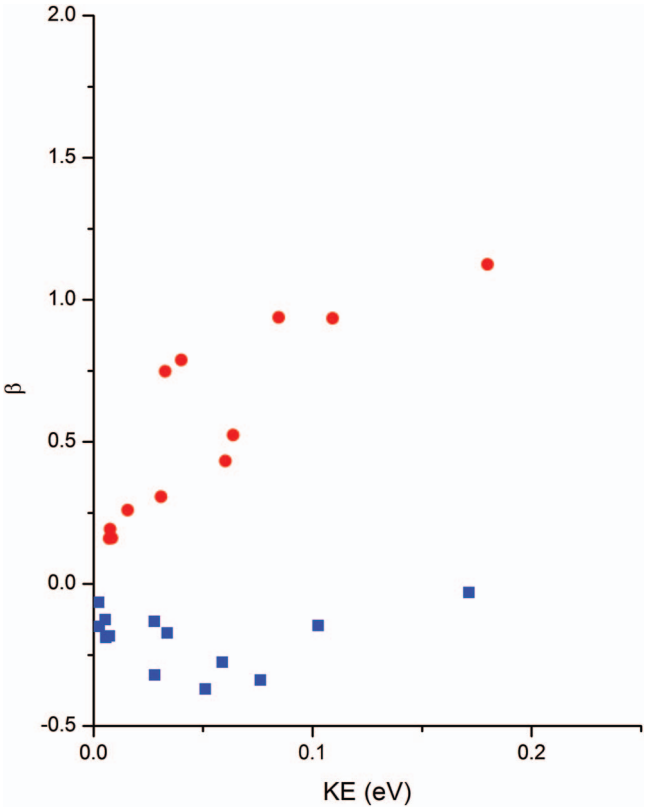

FIG. 4. The anisotropy parameter (β) and its dependence on the kinetic energy for the vibrational peaks resolved for band X in Figs. 2 and 3. Red dots are for the a_1–h_1 peaks and the blue squares for peaks a_2–g_2. Note the different angular distributions of the two sets of peaks, which correspond to two different electronic states.

TABLE II. Observed binding energies from the high-resolution photoelectron spectra of AuC_2^- (Figs. 2 and 3). The signs for the anisotropy parameter (β) are indicated (see also Figure 4).

	Binding energies[a]		
Observed peaks	eV	cm^{-1}	β
hb	3.1954	25 773	
a_1	3.2192	25 965	>0
a_2	3.2213	25 981	<0
b_1	3.2437	26 162	>0
b_2	3.2468	26 187	<0
c_1	3.2674	26 353	>0
c_2	3.2722	26 392	<0
x_1	3.2739	26 406	<0
d_1	3.2909	26 543	>0
d_2	3.2975	26 596	<0
x_2	3.2994	26 611	<0
e_1	3.3154	26 741	>0
e_2	3.3239	26 809	<0
x_3	3.3263	26 828	<0
f_1	3.3398	26 937	>0
f_2	3.3490	27 011	<0
g_1	3.3643	27 135	>0
a_3	3.3716	27 194	<0
g_2	3.3790	27 254	<0
h_1	3.3872	27 319	>0
A	3.4483	27 812	<0
i_1	3.5725	28 814	>0
i_2	3.5753	28 837	<0
j_1	3.5932	28 981	>0
j_2	3.5953	28 998	<0
k_1	3.6115	29 128	>0[b]
K_2	3.6139	29 148	
l	3.6659	29 567	<0

[a]The peak positions have an uncertainty of 0.0007 eV.
[b]Average of the two peaks because they are not well separated.

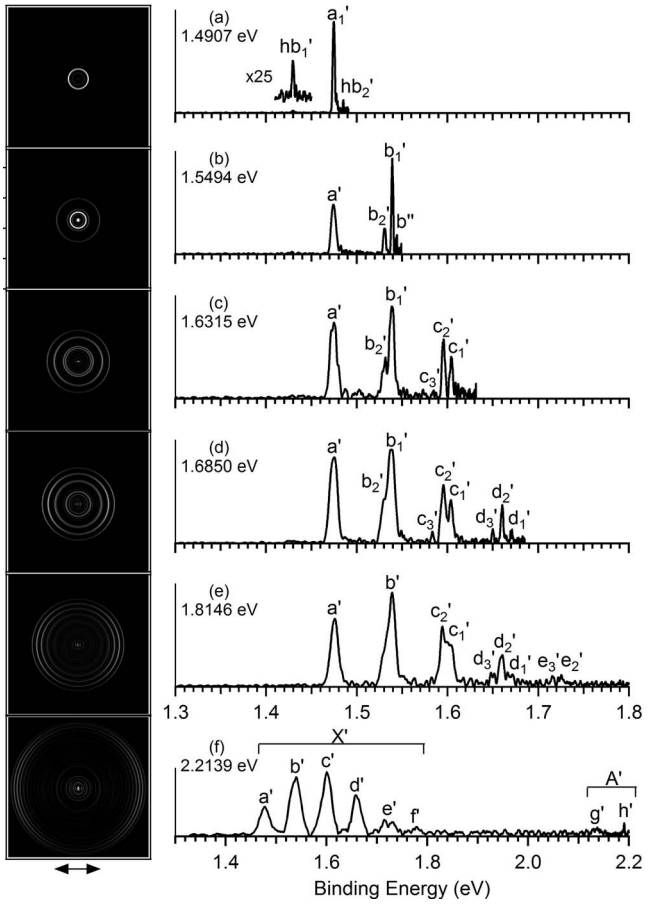

FIG. 5. High resolution photoelectron images and spectra of the minor species of AuC_2^- at detachment photon energies of (a) 1.4907 eV, (b) 1.5494 eV, (c) 1.6315 eV, (d) 1.6850 eV, (e) 1.8146 eV, and (f) 2.2139 eV. The left panels show the photoelectron images after inverse-Abel transformation. The double arrow indicates the polarization of the laser.

the two different electronic states. Clearly, the β parameter for features a_1–h_1 follows the same pattern: they show almost isotropic distributions at lower kinetic energies and the β parameter increases with the kinetic energy, resulting in parallel PAD at higher kinetic energies. On the other hand, the β parameter for features a_2–g_2 is negative in the same kinetic energy range.

The binding energies for all the observed peaks in Figs. 2 and 3 are summarized in Table II. Accurate ADEs and VDEs from the high-resolution imaging data for all the resolved electronic states associated with bands X, A, and B are given in Table I.

C. High-resolution imaging of band X′ from the electronically excited AuC_2^-

Fig. 5 shows the high-resolution PE images and spectra for the weak X′ band in Fig. 1(a). The electron count rates for these spectra were extremely low (between 0.1 and 0.5 count per laser shot). Nevertheless we were able to obtain good quality images with longer data accumulation times. The spectrum at 2.2139 eV photon energy (Fig. 5(f)) agrees well with that reported in Ref. 13, except that the spectral resolution and signal-to-noise ratios are significantly improved in the current data. Furthermore, the hot band in the current data is almost negligible, suggesting that our cluster beam was vibrationally cold. A main vibrational progression consisting of six well-resolved peaks (labeled as a'–f') is observed with an average spacing of about 525 cm^{-1}, in agreement with the 528 cm^{-1} spacing reported in Ref. 13. Additionally, two very weak features are also discernible at 2.1371 eV (labeled as g') and 2.1908 eV (labeled as h'), which correspond to the band A′ in Fig. 1(a). These features are due to additional detachment channels from the meta-stable excited state of AuC_2^-. However, because of their weak relative intensities, these features will not be discussed further.

Interestingly, under high-resolution when the detachment laser is tuned close to each of the vibrational peaks in band X′, fine features are further resolved. In particular, three fine features are resolved for the peaks b′, c′, and d′. For peak a′, a strong sharp peak is observed at 1.4747 eV with a weak peak resolved on the higher binding energy side (hb_2') at the detachment energy of 1.4907 eV (Fig. 5(a)). A very weak hot band (hb_1') is observed, which is separated from peak a_1' by 365 cm^{-1}. The weak peak labeled as hb_2' is separated from

TABLE III. Observed binding energies for detachment transitions from the metastable excited state of AuC_2^- (Fig. 5). The signs for the anisotropy parameter (β) are indicated (see also Fig. 6).

	Binding energies[a]		
Observed peaks	eV	cm^{-1}	β
hb_1'	1.4295	11 529	
a_1'	1.4747	11 894	>0
hb_2'	1.4850	11 977	
b_2'	1.5304	12 343	>0
b_1'	1.5392	12 414	>0
b''	1.5436	12 450	
c_3'	1.5837	12 773	>0
c_2'	1.5957	12 870	>0
c_1'	1.6041	12 938	>0
d_3'	1.6498	13 307	>0
d_2'	1.6603	13 391	>0
d_1'	1.6705	13 473	>0
e_3'	1.7157	13 838	>0
e_2'	1.7255	13 917	>0

[a]The peak positions have an uncertainty of 0.0007 eV.

peak b_2' by exactly the same amount (366 cm^{-1}), suggesting that it should correspond to a hot band for b_2'. These observations imply that both a_1' and b_2' represent origins of separate detachment transitions. The detailed assignments of these spectra will be done in Sec. IV C, where we will show that our assignments are different from that made in Ref. 13. The binding energies of all the resolved peaks in Fig. 5 are collected in Table III.

Fig. 6 shows the dependence of the β parameter with the photoelectron kinetic energy for all the resolved peaks in Fig. 5. All the β values seem to follow the same trend, suggesting they have the same electronic origin. While the PADs lie parallel to the laser polarization at higher kinetic energies, they show almost isotropic distributions at lower kinetic energies.

D. Theoretical results

Extensive calculations were done by Visser *et al.* on AuC_2^- and AuC_2, accompanying their PE imaging work previously.[13] We carried out further DFT calculations to facilitate the interpretation of our new PES data. We have optimized different types of structures for AuC_2 and AuC_2^- and found only the linear or bent Au–C–C arrangements to be relevant, in agreement with the results reported in Ref. 13. Fig. 7 displays the main results of our calculations. We also find that the global minimum of AuC_2^- is linear ($C_{\infty v}$, $^1\Sigma^+$), while the neutral ground state is bent (C_s, $^2A'$) derived from removal of an electron from the 18σ HOMO of AuC_2^- (corresponding to a $^2\Sigma^+$ state in the linear geometry). The first excited state of neutral AuC_2 is linear ($^2\Pi_i$), derived from removal of a 9π electron. The energetics of the two neutral states with respect to the anion global minimum are calculated to be 3.14 and 3.53 eV, respectively. Additionally, two triplet excited states are also found for the AuC_2^- anion: a bent state (C_s, $^3A'$) derived from exciting a 18σ electron to the 19σ

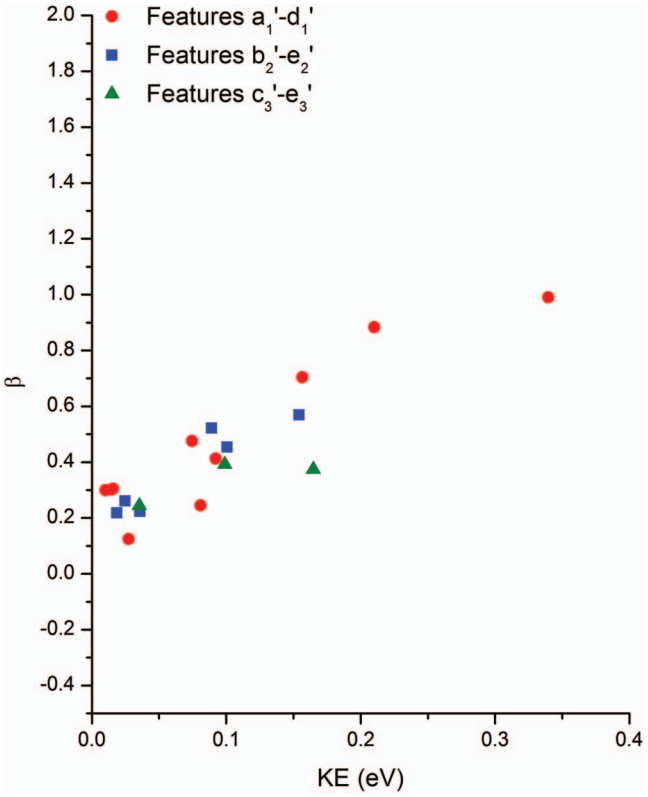

FIG. 6. The anisotropy parameter (β) and its dependence on the kinetic energy for the resolved fine features in Fig. 5. Note that all the resolved peaks show similar angular distributions, indicating their common electronic origin.

LUMO (corresponding to a $^3\Sigma^+$ state in the linear geometry) and a linear state ($^3\Pi_i$) derived from exciting a 9π electron to the 19σ LUMO. These two states are calculated to be 1.96 and 1.97 eV above the anion ground state, respectively.

The relative energies, geometrical parameters, and vibrational frequencies of the computed states for AuC_2^- and AuC_2 are collected in Table IV, where they are compared with those from Ref. 13 at the CCSD(T) level. Overall, the current DFT results agree well with the previous CCSD(T)

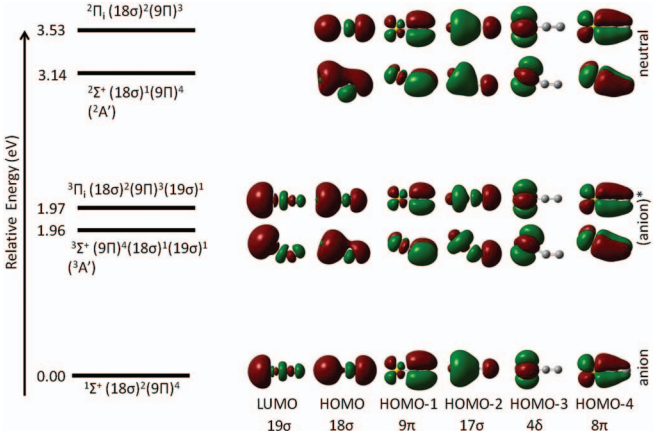

FIG. 7. The computed energies in eV of the two triplet excited states of AuC_2^- and the ground and first excited states of AuC_2 relative to the anion ground state, and their valence molecular orbitals at the DFT level.

TABLE IV. Relative energies (eV), vibrational frequencies (cm^{-1}), and geometrical parameters of AuC_2^- and AuC_2 calculated by DFT method using B3LYP and basis set 6-31++g(d,p) for C and Lanl2dz for Au.[a]

Structure	Relative energy (eV)	ν_1 (Au–C stretch) (cm^{-1})	ν_2 (Au–C–C bend) (cm^{-1})	ν_3 (C–C stretch) (cm^{-1})	Au–C distance (Å)	C–C distance (Å)	Au–C–C angle (°)
Au–C–C$^-$ ($^1\Sigma$)	0.00 (0.00)	460 (457)	214 (190)	1928 (1830)	1.95 (1.93)	1.26 (1.29)	180 (180)
Au–C–C$^-$ ($^3A'$)	1.96 (1.15)	365 (427)	115 (122)	1725 (1659)	2.04 (2.01)	1.30 (1.31)	155 (147)
Au–C–C$^-$ ($^3\Pi$)	1.97 (1.18)	352 (398)	164 (184)	1777 (1732)	2.03 (1.99)	1.30 (1.32)	180 (180)
Au–C–C ($^2A'$)	3.14 (2.65)	497 (534)	204 (204)	1638 (1541)	1.92 (1.93)	1.28 (1.29)	155 (146)
Au–C–C ($^2\Pi$)	3.53 (2.81)	475 (480)	228 (193)	1812 (1743)	1.92 (1.91)	1.30 (1.32)	180 (180)

[a]Values in parentheses are from Ref. 13.

results in terms of the structures and vibrational frequencies. However, the relative energies of the anion excited states and the neutral states seem to be significantly higher in the current calculations. The excited states of the anion in Ref. 13 were calculated to be at 1.15 eV ($^3A'$) and 1.18 eV ($^3\Pi_i$) compared to the current values of 1.96 and 1.97 eV, respectively. The energies of the neutral states relative to the anion ground state were calculated to be 2.65 eV ($^2A'$) and 2.81 eV ($^2\Pi_i$) in Ref. 13 in comparison to the current values of 3.14 and 3.53 eV, respectively. For the $^3\Sigma^+$ excited state in the anion and the $^2\Sigma^+$ ground state in the neutral, the linear structure is found to be a transition state with an imaginary frequency, resulting in the bent structures in agreement with Visser *et al.*[13]

IV. DISCUSSION

A. Photoelectron spectrum at 193 nm: Observation of a metastable excited state of AuC_2^-

The simulated spectrum from the $^1\Sigma^+$ ground state of AuC_2^- (Fig. 1(b)) agrees qualitatively with the main experimental features. The valence MOs for the $^1\Sigma^+$ ground state of AuC_2^- are shown in Fig. 7. The 18σ HOMO is an Au–C antibonding orbital between the Au 6s and the C_2 σ orbital, corresponding to the X band in the 193 nm spectrum (Fig. 1(a)). The antibonding nature of the 18σ orbital is reflected from the shortened Au–C bond distance and the increased Au–C stretching frequency in the neutral ground state relative to the anion ground state (Table IV). The 9π orbital is mainly the C_2 π bonding orbital with weak anti-bonding interactions with the Au 5dπ orbital. Detachment from this MO gives rise to band A in the 193 nm spectrum. The 17σ orbital is a strong Au–C bonding orbital, corresponding to band B in the 193 nm spectrum. The calculated VDEs from these three orbitals without spin-orbit effects are very close to each other, in agreement with the congested nature of bands X, A, and B (Fig. 1(a)). Following a large energy gap, band C is from detachment from the nonbonding 4δ orbital. Band C is very sharp, suggesting little structural change upon electron detachment, consistent with the nonbonding nature of the 4δ orbital. Finally, the D band is from detachment of the 8π orbital, which is a strong Au–C π bonding orbital, in agreement with the apparent broad width of this band.

Fig. 1(c) displays the simulated spectra from the two excited states of AuC_2^-. Both states give rise to low binding energy features, consistent with the weak X′ and A′ signals observed in the 193 nm. Weak photoelectron signals also seem to exist between 4 and 5 eV (Fig. 1(a)), which should come from higher binding energy detachment channels from the excited states of AuC_2^-. Visser *et al.* assigned their PE images to detachment from the $^3A'$ ($^3\Sigma^+$) excited state of AuC_2^-, corresponding to the X′ band.[13] As will be shown below, our high-resolution data reveal unequivocally that the weak signals come from the $^3\Pi$ excited of AuC_2^-. On the basis of the relative intensities, we estimate that the $^3\Pi$ state was populated with no more than ~2% relative to the ground state of AuC_2^-. However, it is surprising that such a highly excited state was populated at all in our experiment, because our cluster beam was fairly cold, as can be seen by the negligible vibrational hot bands. Franck-Condon simulations to be discussed later suggest a vibrational temperature of ~125 K. Hence, the population of the triplet excited state of AuC_2^- was non-Boltzmann and it should be a result of the metastability of the triplet excited state, which is spin-forbidden to relaxing down to the singlet ground state of AuC_2^- in the cluster source. We have observed previously such "spin-protected" metastable excited states in a number of molecular and cluster anions produced from our laser vaporization source.[28–31] Laser vaporization is a highly nonthermal process. Apparently, metastable anions can be produced, which survive the collisions in the cluster source and the subsequent supersonic expansion. However, such higher energy species, if present at all, are usually populated in very small quantities and are usually negligible in PES. The fact that we can sometime detect them at all is testimony to the high sensitivity of the magnetic-bottle PES technique and the PE imaging method.

B. High-resolution PE imaging of the global minimum linear AuC_2^- ($^1\Sigma^+$)

1. The X and A bands: The bent ground state and spin-orbit splitting of the $^2\Pi$ excited state

Even though the X band is assigned to the electron detachment from the 18σ HOMO on the bases of the low resolution 193 nm spectrum and the theoretical VDE (Fig. 1), high-resolution data presented in Figs. 2 and 3 show that this band in fact consists of two closely-lying electronic states with different bending frequencies. The ground state consists of an extensive bending progression with a frequency of 195 cm^{-1}, compared with the calculated bending frequency of 204 cm^{-1} (Table IV). The calculation gives an equilibrium bond angle

of 155° for the ground state (C_s, $^2A'$), which is from detachment of a 18σ electron. The nature of this detachment transition is confirmed from both the threshold behavior of the vibrational features and their angular distributions.

Fig. 3 shows that the vibrational peaks (a_1-e_1) of the ground state exhibit a drastic reduction in intensity near threshold. This is a consequence of the Wigner's threshold law,[32] which biases against outgoing electrons with angular momentum $l > 0$ near threshold, i.e., for low energy electrons. To illustrate the dramatic change in intensity of the ground state vibrational peaks near threshold, we took photoelectron images by varying the detachment photon energies (or kinetic energies of the outgoing electrons) at small steps between 3.3001 and 3.3201 eV, as shown in Fig. 8. At 3.3001 eV (Fig. 8(a)), the d_1 peak near threshold is negligible, whereas the c_1 peak, which is away from threshold, has similar intensity as the c_2 peak from the first excited state. As the photon energy increases, the intensity of both the c_1 and d_1 peak increase. A dashed line is drawn in Fig. 8 to guide the eyes for the d_1 peak. Fig. 8(d) shows that near threshold the e_1 vibrational peak for the ground electronic state of AuC_2 also has negligible intensity. These observations suggest that the outgoing electrons have angular momentum > 0, consistent with detachment from the 18σ HOMO, which would yield electrons with $l = 1$ as p-waves. The β parameters for the ground state vibrational levels and their dependence on kinetic energies, shown in Fig. 4, are consistent with primarily p-wave characters for the outgoing electrons.

The closely-lying first excited state of AuC_2 consists of a similarly extensive bending progression (a_2-e_2 in Fig. 3) as the ground state, but its bending frequency of 207 cm^{-1} is slightly higher. Both the threshold behavior (Figs. 3 and 8) and the β parameters for the excited state vibrational features are opposite to those of the ground state and are consistent with detachment from the 9π orbital, which would produce outgoing electrons with $l = 0$ (s-wave) or 2 (d-wave). The β parameter for the single peak corresponding to band A (Fig. 2) is similar to that of the first excited state. Thus, they should have the same origin and are assigned to the two spin-orbit components of the $^2\Pi$ excited state owing to electron detachment from the 9π orbital of AuC_2^-. The A band should correspond to the $^2\Pi_{1/2}$ state, corresponding to a linear structure with little change relative to the anion ground state. However, the $^2\Pi_{3/2}$ component is shown to be bent, similar to the ground state. The observation that the two spin-orbit states have very different structures and spectroscopic properties is unusual, which is a result of strong $^2\Sigma^+$–$^2\Pi$ and spin-orbit vibronic coupling to be discussed next. Fig. 9 shows schematically the double-well bending potentials of the ground and first excited state of AuC_2 and the harmonic potential of the $^2\Pi_{1/2}$ excited state. The vibrational levels for the two double-well potentials are also drawn schematically, according to the resolved vibrational features in Figs. 2 and 3. The vibrational levels above the barrier of the double-well potentials are expected to become more closely-spaced, consistent with the complicated fine features resolved for peak g in Fig. 2. This part of the spectra should be above the bending barrier. These complicated spectral features are also a direct consequence of the strong $^2\Sigma^+$–$^2\Pi$ and spin-orbit vibronic coupling.

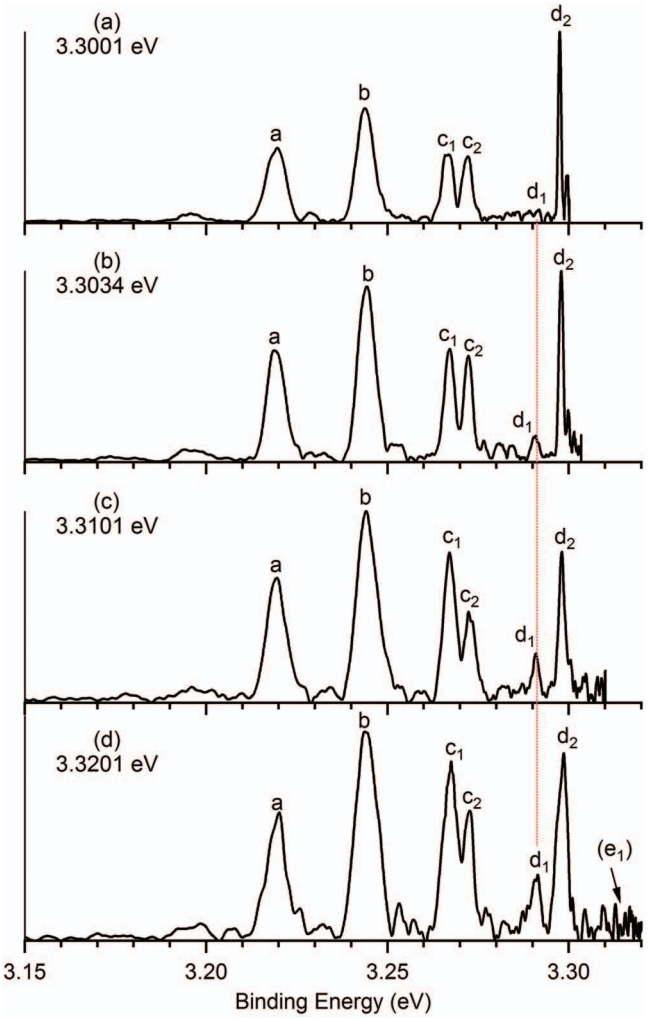

FIG. 8. Photoelectron spectra of AuC_2^- at detachment photon energies of (a) 3.3001 eV, (b) 3.3034 eV, (c) 3.3101 eV, and (d) 3.3201 eV, showing the different threshold behaviors of peaks d_1 and d_2. The vertical dashed line is simply to guide the eyes.

2. Strong $^2\Sigma^+$–$^2\Pi$ and spin-orbit vibronic coupling

The degenerate $^2\Pi$ excited state of AuC_2 is unstable against bending vibrations due to the Renner-Teller effect.[33,34] However, why is the ground state of AuC_2 bent, which corresponds to a nondegenerate $^2\Sigma^+$ state in the linear geometry? It turns out that interactions between different electronic states, leading to the breakdown of the Born-Oppenheimer approximation, have been found to be important in many linear molecules.[34–38] The theory of vibronic coupling in linear molecules has been well developed.[33–35,38–40] In particular, vibronic coupling between Σ and Π states has been found in many triatomic molecules. Domcke and co-workers have specifically developed the theoretical frameworks for strong $^2\Sigma$–$^2\Pi$ and spin-orbit vibronic couplings,[41] showing that both the $^2\Pi_{3/2}$ and $^2\Sigma$ states can be bent in strong coupling cases, while the $^2\Pi_{1/2}$ state remains linear. This is exactly in agreement with the current observation in AuC_2. Domcke and co-workers[42] even calculated vibronic structures of photodetachment spectra of linear $ClCC^-$ and $BrCC^-$ to the neutral $^2\Sigma^+$ ground state and first

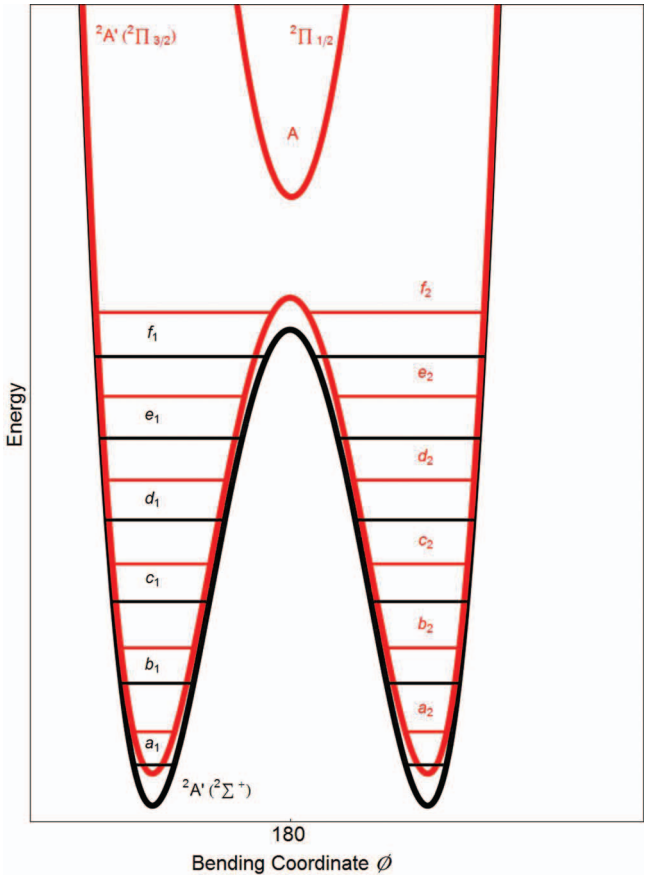

FIG. 9. Schematic potential energy curves of the ground state ($^2\Sigma^+$ in black), the first excited state ($^2\Pi_{3/2}$ in red), and the second excited state ($^2\Pi_{1/2}$) of AuC_2 along the bending coordinate, showing the double-well potentials for the $^2\Sigma^+$ and $^2\Pi_{3/2}$ states due to strong vibronic coupling. The vibrational levels for the $^2\Sigma^+$ (black) and $^2\Pi_{3/2}$ (red) states are labeled according to the photoelectron spectra of Figs. 2 and 3.

$^2\Pi$ excited states, very similar to the current AuC_2^- case, even though there have been no experimental data available for the halogen XC_2^- species.

Well-resolved photodetachment spectra for linear triatomic species containing a C_2 unit are only available for C_2H^-,[43,44] which involves detachment to a $^2\Sigma^+$ ground state and a $^2\Pi$ excited state of neutral C_2H and can be viewed to be similar to AuC_2^-. Vibronic coupling was observed in the ground state of C_2H in the photodetachment spectra. However, the vibronic coupling is relatively weak and the ground state of C_2H remains linear, because of the relatively large separation between the $^2\Pi$ and $^2\Sigma^+$ states.[43,44] In addition, the spin-orbit effect is negligible in the $^2\Pi$ state of C_2H. Hence, the AuC_2 molecule provides an ideal system to investigate the Σ–Π and spin-orbit vibronic coupling and our high-resolution PES data warrant further theoretical studies. The high-resolution photodetachment data can be used to compare with calculated vibronic structures and allow the coupling constant to be obtained. As will be shown below in Sec. IV C, the spin-orbit coupling constant in the $^2\Pi$ state at the linear geometry in AuC_2 (Fig. 10), which would be important in the vibronic coupling calculations, is accurately measured in the high-resolution photodetachment data for the weakly populated excited state of AuC_2^-.

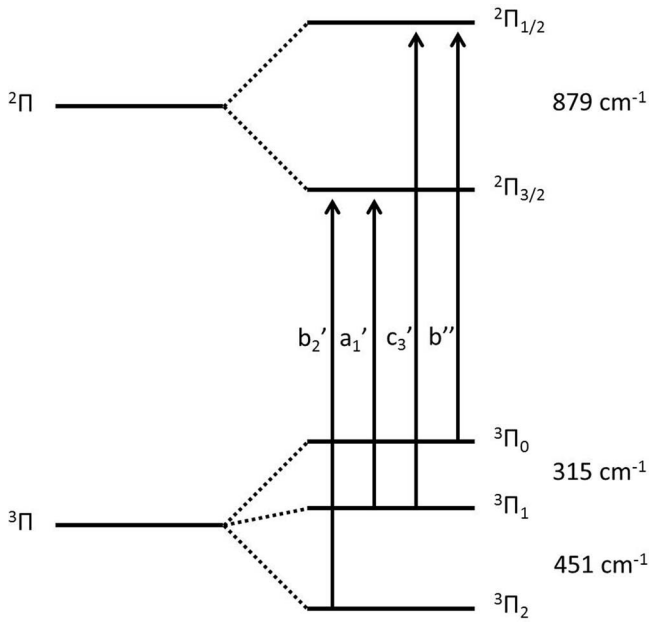

FIG. 10. Energy level diagrams for the spin-orbit splitting of the $^3\Pi$ excited state of AuC_2^- and the $^2\Pi$ state of AuC_2. The allowed transitions and the assignments for the observed fine features in Fig. 5 are indicated by the arrows. The obtained spin-orbit parameters are given in cm^{-1}.

3. Band B: Another bent state corresponding to a $^2\Sigma^+$ linear state?

Band B is due to detachment from the 17σ orbital (Fig. 2), which is a strong Au–C bonding orbital involving Au 6*s* and the C_2 σ^* orbitals (Fig. 7). This detachment channel should lead to a $^2\Sigma^+$ excited state of AuC_2. Hence, a vibrational progression in the Au–C stretching mode would be expected. However, the observed vibronic structures (*i*–*l* in Fig. 2(a)) do not correspond to a stretching progression. The *i*, *j* *k* peaks seem to correspond to a short and highly anharmonic bending progression, suggesting that the $^2\Sigma^+$ excited state may also be bent with a shallow double-well potential curve. The peak *l*, which does not represent a regular spacing to the bending progression, may be due to a vibrational level above the bending barrier, similar to the peak *g* in the X band (Fig. 2(a)). The splitting of the *i*, *j*, *k*, peaks into doublet (inset in Fig. 2(a)) is even more puzzling. This splitting could be caused by an asymmetric double-well potential, as schematically shown in Fig. 12. Since the $^2\Sigma^+$ excited state is relatively close in energy to the $^2\Pi_{1/2}$ state, it raises the specter of a strong $^2\Sigma^+$–$^2\Pi$–$^2\Sigma^+$ and spin-orbit vibronic coupling, which can conceivably cause the upper $^2\Sigma^+$ state to bend. To our knowledge, there has been no theoretical consideration of such a complicated four-state vibronic and spin-orbit coupling.

C. High-resolution PE imaging of the metastable triplet excited state of AuC_2^-

1. The X′ band

The low-resolution PE image of band X′ at 2.2139 eV photon energy (Fig. 5(f)) shows a progression with a spacing

of ~525 cm^{-1}, consistent with the calculated Au–C stretching mode of both the $^2\Sigma^+$ and $^2\Pi$ final states of AuC_2 (Table IV). This spectrum agrees well with that by Visser *et al.*,[13] who assigned the transition to be from the metastable $^3A'$ ($^3\Sigma^+$) excited state of AuC_2^- to the $^2A'$ ground state of AuC_2 (Fig. 7). They ruled out the $^2\Pi \leftarrow {}^3\Pi$ transition, because the expected 500 cm^{-1} spin-orbit splitting was not observed. However, our high-resolution data in Fig. 5 revealed fine features, which consist of several series of vibrational peaks with similar Au–C stretching frequencies and are consistent with transitions involving different spin-orbit states from the $^3\Pi$ anionic state to those of the $^2\Pi$ neutral final state.

A careful analysis of the high-resolution spectra in Fig. 5 indicates that there are three vibrational progressions and possibly a fourth one. The features a_1', b_1', c_1', and d_1' consist of the lowest energy series with a vibrational spacing of 528 ± 8 cm^{-1}. The very weak peak labeled as hb_1' represents a hot band of this series, giving rise to an Au–C stretching frequency of 365 cm^{-1} for the metastable triplet state of AuC_2^-. The peak b_2' at 1.5304 eV appears at 449 cm^{-1} above a_1' and this peak forms another series with c_2', d_2', and e_2' with a vibrational spacing of 524 ± 5 cm^{-1}. The weak peak labeled as hb_2' resolved in Fig. 5(a) represents the hot band for this series, giving rise to an Au–C stretching frequency of 366 cm^{-1} for the metastable triple state of AuC_2^-, the same as that obtained from the hb_1' peak relative to the a_1' series. Thus, the a_1' and b_2' peaks represent unequivocally distinct electronic transitions from the metastable triplet state of AuC_2^-. In addition, we observe a relatively weak third series, consisting of c_3', d_3', and e_3' with a vibrational spacing of 532 ± 10 cm^{-1}. The origin peak c_3' is measured to be 879 cm^{-1} above feature a_1' and thus 430 cm^{-1} above peak b_2'.

These three vibrational progressions all have similar Au–C stretching frequencies without any evidence of bending vibrations. In addition, the separation between the origins of these progressions are on the order of the spin-orbit couplings estimated for the $^3\Pi$ excited state of AuC_2^-.[13] Thus, they should be due to transitions from the spin-orbit states of the linear $^3\Pi$ excited state of AuC_2^- to those of the linear $^2\Pi$ state of neutral AuC_2, as shown in Fig. 10 schematically. The lowest energy allowed transition is $^2\Pi_{3/2} \leftarrow {}^3\Pi_1$, corresponding to the a_1' progression. The spin-orbit splitting between the $^3\Pi_2$ and $^3\Pi_1$ and between $^3\Pi_1$ and $^3\Pi_0$ are 451 cm^{-1} and 315 cm^{-1}, respectively, as shown in Fig. 10. Interestingly, we are also able to determine the spin-orbit splitting constant of the $^2\Pi$ excited state of the neutral AuC_2 at the linear geometry as 879 cm^{-1}. According to this assignment, there should also be an allowed transition, $^2\Pi_{1/2} \leftarrow {}^3\Pi_0$. Indeed, a weak peak b″ is resolved in Fig. 5(b), which has the correct energy for this transition (Table III). The weak intensity of the b″ peak is expected because the $^3\Pi_0$ spin-orbit state has the highest energy and its population should be the weakest.

The $^2\Pi_i \leftarrow {}^3\Pi_i$ transitions involve removal of the electron in the 19σ orbital (Fig. 7), which is primarily the Au 6*s* orbital with some weak anti-bonding contribution from the C_2 σ orbital. The outgoing electrons should be primarily of *p*-wave character. The β parameters of the different vibrational peaks for the X′ band and their kinetic energy dependence follow the same trend, suggesting these peaks have the same electronic origin. The β parameters are all positive and increase with kinetic energies, consistent with their *p*-wave characters.

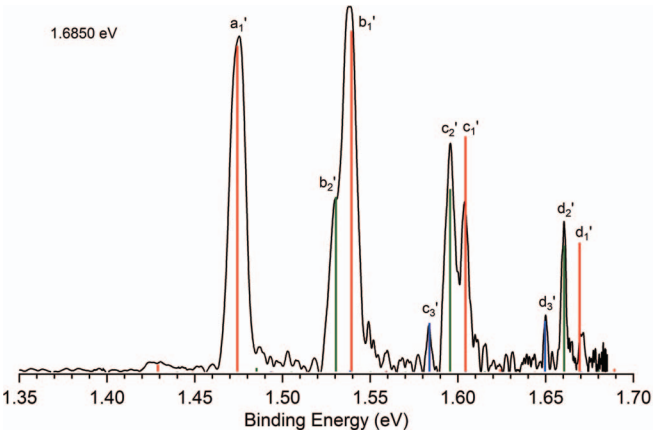

FIG. 11. Comparison of the calculated Franck-Condon factors for the detachment transitions from the $^3\Pi$ excited state of AuC_2^- with the photoelectron spectrum at 1.6850 eV (Fig. 5(d)). A vibrational temperature of 125 ± 25 K was obtained. The red, green and blue colors are used to indicate the $^2\Pi_{3/2} \leftarrow {}^3\Pi_1$, $^2\Pi_{3/2} \leftarrow {}^3\Pi_2$, and $^2\Pi_{1/2} \leftarrow {}^3\Pi_1$ transitions, respectively.

2. Vibrational temperature

Because of the strong vibronic coupling in the detachment transitions to the $^2A'$ ($^2\Sigma^+$) ground state and the $^2A'$ ($^2\Pi_{3/2}$) excited state, the observed bending vibrational progressions cannot be fitted with Franck-Condon (FC) factors to obtain spectroscopic constants and vibrational temperatures.[32] On the other hand, the transitions from the $^3\Pi_i$ metastable states to the $^2\Pi_i$ neutral states only involve linear structures and the Au–C stretching mode. Since the stretching coordinate does not involve in vibronic couplings, we carried out FC simulations for the PE spectra of the metastable state to estimate the vibrational temperature of the anion. The simulation was done using the Pescal program,[45] which computes FC factors by numerical integration of vibrational wavefunctions of a Morse oscillator. Fig. 11 shows the comparison of the experimental spectrum taken at 1.6850 eV (Fig. 5(d)) with the simulated FC factors, which were assumed to be the same for the three transitions involving different spin-orbit states. The spectroscopic values employed are ω_e = 365 cm^{-1} and r = 2.05 Å for the $^3\Pi$ excited state of the anion, and r = 1.92 Å with ω_e = 526 and 532 cm^{-1} for the frequencies of the $^2\Pi_{3/2}$ and $^2\Pi_{1/2}$ neutral states, respectively. We obtained a vibrational temperature of 125 ± 25 K by fitting the calculated FC to the hot band off the a_1' peak. The fitting is not perfect, in particular, for the c_1' and d_1' peaks, most likely due to the reduced detachment cross sections for low energy electrons as a result of the Wigner threshold law.[32]

3. Energy levels of AuC_2^- and AuC_2

A wealth of spectroscopic information is obtained for AuC_2^- and AuC_2 in the current work. The electron binding

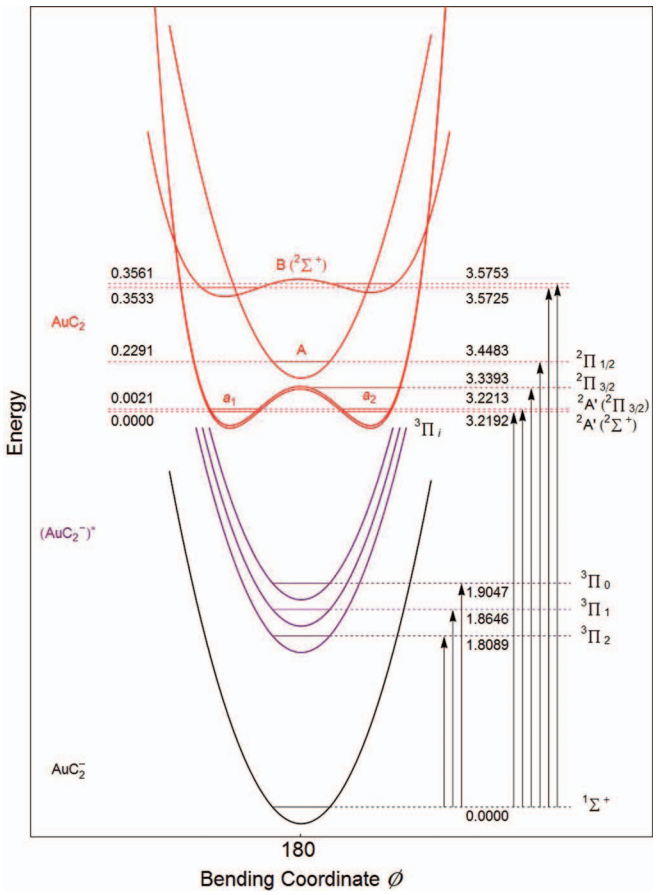

FIG. 12. Schematic energy levels and bending potential energy curves for the ground state (black) and the spin-orbit split $^3\Pi$ excited states (purple) of AuC_2^-, and the four neutral states (red). The measured energies relative to the anion ground state are shown on the right and indicated by the arrows. The obtained excitation energies of the neutral excited states relative to the neutral ground state are given on the left.

energies for all the observed detachment transitions are given in Tables II and III. The energy level diagram in Fig. 12 summarizes schematically all the energetic and spectroscopic information obtained. The double-well potential for the $^2\Sigma^+$ excited state of AuC_2 is drawn asymmetrically to account for the observed splittings in the high-resolution PE spectrum (inset in Fig. 2).

D. Comparison of the chemical bonding in Au–CC$^-$ with ClAu–CCH$^-$

Recently, we studied the gold-carbon bonds in different gold-alkynyl complexes.[10] The Au–C bond strength in ClAu–CCH$^-$ was shown to be extremely high (5.01 eV for ClAu–CCH$^-$ to dissociate to ClAu + CCH$^-$ calculated at the CCSD(T) level), even higher than that in ClAuCN$^-$. More surprisingly, it was found that the single Au–C bond in ClAu–CCH$^-$ was stronger than the Au=C and Au≡C multiple bonds, revealing an inverse correlation between bond strength and bonder order. The strong Au–C bond in ClAu–CCH$^-$ was shown to be due to the polarization effect of the electronegative Cl: the Au–C bond in FAu–CCH$^-$ was shown to be even stronger, while that in IAu–CCH$^-$ was weaker.[10] The calculated Au–C distance of 1.95 Å in AuC_2^- (Table IV) is the same as that in ClAu–CCH$^-$. But the Au–C stretching frequency in AuC_2^- is lower than that in ClAu–CCH$^-$. We calculated the dissociation energy of AuC_2^- ($^1\Sigma^+$) → Au (^{2}S) + C_2^- ($^2\Pi_u$) to be ~3.10 eV at the B3LYP/ECP level, which is significantly smaller than the 4.52 eV or 5.23 eV dissociation energies for ClAu–CCH$^-$ ($^1\Sigma^+$) → ClAu ($^1\Sigma^+$) + CCH$^-$ ($^1\Sigma^+$) or ClAu–CCH$^-$ ($^1\Sigma^+$) → ClAu$^-$ ($^2\Sigma^+$) + CCH ($^2\Sigma^+$), respectively, calculated at the same level of theory (B3LYP/ECP). These results show again the importance of the auxiliary ligand (L) in influencing the Au–C bond in LAu–CCH$^-$. The bonding in AuCCH or AuCCH$^-$ would provide even better references to assess the influence of L on the Au–C bonding in LAu–CCH$^-$.

Transition metal atoms tend to bond with C_2 in side-on fasion[46–48] because of the strong interactions between the metal *d* orbitals and the C_2 π orbitals, whereas there is a competition between side-on and terminal bonding for Al with C_2.[49,50] The terminal bonding of Au with C_2 is more analogous to H. In previous studies, we have found an analogy between Au and H in their bonding to Si or B.[51–56] Thus, the AuC_2^- molecule can be viewed to be analogous to HC_2^- and it provides an example of the Au/H analogy in the Au–C bonding.

V. CONCLUSIONS

We report high-resolution photoelectron spectroscopy and imaging of AuC_2^- at a wide photon energy range. The 193 nm spectrum revealed five major detachment bands, as well as very weak low binding energy features due to a metastable excited state of AuC_2^-. The ground state of AuC_2^- is linear ($^1\Sigma^+$), but the neutral ground state, corresponding to a $^2\Sigma^+$ state at the linear geometry, is shown to be bent, as a result of strong vibronic interactions with the nearby $^2\Pi$ excited state with strong spin-orbit coupling. The electron affinity of AuC_2 is measured to be 3.2192(7) eV and the ground state bending frequency is measured to be 195(6) cm^{-1}. The first excited state of AuC_2 corresponding to the $^2\Pi_{3/2}$ spin-orbit state is also bent due to the strong vibronic coupling. It is above the AuC_2 ground state by only 0.0021 eV and has a bending frequency of 207(6) cm^{-1}. The $^2\Pi_{1/2}$ state is shown to be linear with an excitation energy of 0.2291 eV relative to the neutral ground state. A $^2\Sigma^+$ excited state, 0.3533 eV above the ground state, is also found to be bent, possibly due to vibronic interactions with the lower $^2\Pi$ states. The metastable excited state of AuC_2^- is shown to be populated less than 2% compared to the main isomer. High-resolution PE imaging data show that this state is a $^3\Pi$ state and all the allowed transitions from the spin-orbit states ($^3\Pi_{2,1,0}$) to the neutral $^2\Pi_{3/2}$ and $^2\Pi_{1/2}$ states are observed and the spin-orbit splittings are accurately measured for both the metastable anionic state and the $^2\Pi$ neutral state. The AuC_2 molecule provides a prototype to investigate the $^2\Sigma$–$^2\Pi$ vibronic and spin-orbit coupling in linear molecules. The current high-resolution photoelectron data are ideal to compare with theoretical calculations including vibronic and spin-orbit couplings.

ACKNOWLEDGMENTS

I.L. would like to thank the Basque Government for a postdoctoral fellowship. This work was supported by the National Science Foundation (CHE-1049717).

[1]P. Pyykko, Chem. Rev. **88**, 563 (1988).
[2]H. Schmidbaur, Gold Bull. **33**, 3 (2000).
[3]G. J. Hutchings, M. Brust, and H. Schmidbaur, Chem. Soc. Rev. **37**, 1759 (2008).
[4]L. S. Wang, Phys. Chem. Chem. Phys. **12**, 8694 (2010).
[5]A. S. K. Hashmi, Chem. Rev. **107**, 3180 (2007).
[6]G. J. Gorin, B. D. Sherry, and F. D. Toste, Chem. Rev. **108**, 3351 (2008).
[7]E. Jimenez-Nunez and A. M. Echavarren, Chem. Rev. **108**, 3326 (2008).
[8]Z. G. Li, C. Brouwer, and C. He, Chem. Rev. **108**, 3239 (2008).
[9]A. Corma, A. Leyva-Perez, and M. J. Sabater, Chem. Rev. **111**, 1657 (2011).
[10]H. T. Liu, X. G. Xiong, P. D. Dau, Y. L. Wang, D. L. Huang, J. Li, and L. S. Wang, Nat. Commun. **4**, 2201 (2013).
[11]B. W. Ticknor, B. Bandyopadhyay, and M. A. Duncan, J. Phys. Chem. A **112**, 12355 (2008).
[12]Y. Cohen, V. Bernshtein, E. Armon, A. Bekkerman, and E. Kolodney, J. Chem. Phys. **134**, 124701 (2011).
[13]B. R. Visser, M. A. Addicoat, J. R. Gascooke, W. D. Lawrance, and G. F. Metha, J. Chem. Phys. **138**, 174310 (2013).
[14]A. Sanov and R. Mabbs, Int. Rev. Phys. Chem. **27**, 53 (2008).
[15]D. M. Neumark, J. Phys. Chem. A **112**, 13287 (2008).
[16]I. León, Z. Yang, and L. S. Wang, J. Chem. Phys. **138**, 184304 (2013); **139**, 089903 (2013) [Erratum].
[17]Z. Yang, I. León, and L. S. Wang, J. Chem. Phys. **139**, 021106 (2013).
[18]I. León, Z. Yang, and L. S. Wang, J. Chem. Phys. **139**, 194306 (2013).
[19]L. S. Wang, H. S. Cheng, and J. W. Fan, J. Chem. Phys. **102**, 9480 (1995).
[20]W. Huang and L. S. Wang, Phys. Rev. Lett. **102**, 153401 (2009).
[21]V. Dribinski, A. Ossadtchi, V. A. Mandelshtam, and H. Reisler, Rev. Sci. Instrum. **73**, 2634 (2002).
[22]G. A. Garcia, L. Nahon, and I. Powis, Rev. Sci. Instrum. **75**, 4989 (2004).
[23]M. J. Frisch *et al.*, Gaussian 09, Revision A.2, Gaussian, Inc., Wallingford, CT, 2009.
[24]A. D. Becke, J. Chem. Phys. **98**, 5648 (1993).
[25]C. Lee, W. Yang, and R. G. Parr, Phys. Rev. B. **37**, 785 (1988).
[26]X. Li, B. Kiran, J. Li, H. J. Zhai, and L. S. Wang, Angew. Chem. Int. Ed. **41**, 4786 (2002).
[27]C. N. Yang, Phys. Rev. **74**, 764 (1948).
[28]H. B. Wu, S. R. Desai, and L. S. Wang, J. Phys. Chem. A **101**, 2103 (1997).
[29]S. K. Nayak, B. K. Rao, P. Jena, X. Li, and L. S. Wang, Chem. Phys. Lett. **301**, 379 (1999).
[30]H. J. Zhai, B. Kiran, J. Li, and L. S. Wang, Nat. Mater. **2**, 827 (2003).
[31]A. N. Alexandrova, A. I. Boldyrev, H. J. Zhai, and L. S. Wang, J. Phys. Chem. A **108**, 3509 (2004).
[32]E. P. Wigner, Phys. Rev. **73**, 1002 (1948).
[33]P. Rosmus and G. Chambaud, "The Renner-Teller effect and the role of electronically degenerate states in molecular ions," in *Photoionization and Photodetachment*, edited by C. Y. Ng (World Scientific, Singpore, 2000), Vol. 10A, Chap. 5, pp. 182–245.
[34]I. B. Bersuker, Chem. Rev. **113**, 1351 (2013).
[35]H. Koppel, L. S. Cederbaum, W. Domcke, and W. von Niessen, Chem. Phys. **37**, 303 (1979).
[36]R. T. Wiedmann and M. G. White, J. Chem. Phys. **102**, 5141 (1995).
[37]Y. Sumiyoshi, T. Ueno, and Y. Endo, J. Chem. Phys. **119**, 1426 (2003).
[38]Y. Liu, I. B. Bersuker, W. Zou, and J. E. Boggs, Chem. Phys. **376**, 30 (2010).
[39]H. Koppel, W. Domcke, and L. S. Cederbaum, J. Chem. Phys. **74**, 2945 (1981).
[40]S. Mishra, V. Vallet, L. V. Poluyanov, and W. Domcke, J. Chem. Phys. **123**, 124104 (2005).
[41]S. Mishra, W. Domcke, and L. V. Poluyanov, Chem. Phys. **327**, 457 (2006).
[42]S. Mishra, V. Vallet, L. V. Poluyanov, and W. Domcke, J. Chem. Phys. **125**, 164327 (2006).
[43]K. M. Ervin and W. C. Lineberger, J. Phys. Chem. **95**, 1167 (1991).
[44]T. R. Taylor, C. Xu, and D. M. Neumark, J. Chem. Phys. **108**, 10018 (1998).
[45]K. M. Ervin, PESCAL, Fortran program, 2010.
[46]J. Fan and L. S. Wang, J. Phys. Chem. **98**, 11814 (1994).
[47]X. Li and L. S. Wang, J. Chem. Phys. **111**, 8389 (1999).
[48]H. J. Zhai, S. Liu, X. Li, and L. S. Wang, J. Chem. Phys. **115**, 5170 (2001).
[49]A. I. Boldyrev, J. Simons, X. Li, and L. S. Wang, J. Am. Chem. Soc. **121**, 10193 (1999).
[50]N. A. Cannon, A. I. Boldyrev, X. Li, and L. S. Wang, J. Chem. Phys. **113**, 2671 (2000).
[51]B. Kiran, X. Li, H. J. Zhai, L. F. Cui, and L. S. Wang, Angew. Chem. Int. Ed. **43**, 2125 (2004).
[52]X. Li, B. Kiran, and L. S. Wang, J. Phys. Chem. A **109**, 4366 (2005).
[53]B. Kiran, X. Li, H. J. Zhai, and L. S. Wang, J. Chem. Phys. **125**, 133204 (2006).
[54]H. J. Zhai, L. S. Wang, D. Y. Zubarev, and A. I. Boldyrev, J. Phys. Chem. A **110**, 1689 (2006).
[55]H. J. Zhai, C. Q. Miao, S. D. Li, and L. S. Wang, J. Phys. Chem. A **114**, 12155 (2010).
[56]H. Bai, H. J. Zhai, S. D. Li, and L. S. Wang, Phys. Chem. Chem. Phys. **15**, 9646 (2013).